

Orbital-resolved nonadiabatic tunneling ionizationQingbin Zhang,^{1,2} Gihan Basnayake,¹ Alexander Winney,¹ Yun Fei Lin,¹ Duke Debrah,¹ Suk Kyoung Lee,¹ and Wen Li^{1,*}¹*Department of Chemistry, Wayne State University, Detroit, Michigan 48202, USA*²*School of Physics, Huazhong University of Science and Technology, Wuhan 430074, China*

(Received 7 March 2017; published 25 August 2017)

In this theoretical work, we show that both the orbital helicity (p_+ vs p_-) and the adiabaticity of tunneling have a significant effect on the initial conditions of tunneling ionization. We developed a hybrid quantum (numerical solution of the time-dependent Schrödinger equation) and classical (back propagation of trajectories) approach to extract orbital-specific initial conditions of electrons at the tunneling exit. Clear physical insight connecting these initial conditions with the final momentum and deflection angles of electrons are presented. Moreover, the adiabaticity of tunneling ionization is characterized by comparing the initial conditions with those with a static field. Significant nonadiabatic tunneling is found to persist beyond a Keldysh parameter of less than 0.5.

DOI: [10.1103/PhysRevA.96.023422](https://doi.org/10.1103/PhysRevA.96.023422)**I. INTRODUCTION**

Tunneling ionization is the most fundamental process in strong-field atomic and molecular physics, in which the binding potential is strongly suppressed by the laser electric field and the electrons gain a nonzero probability of escaping (tunneling) to the continuum. The understanding of electron tunneling has laid the foundations for the rapidly growing field of attosecond science [1], because it is the first step of many important phenomena, such as high harmonic generation (attosecond pulse production) and nonsequential double ionization.

Because tunneling is a quantum phenomenon and has no direct classical analog, the determination of the tunneling exit, the initial momentum and the time is intensely debated. However, it has been shown that it is reasonable to classicalize the wave function when the electron has tunneled into the continuum. By assuming classical initial exits and distributions of velocities [2–4], many strong-field ionization experiments [4–6] have been qualitatively interpreted, even though the adopted tunneling initial conditions are far from being unambiguous. Some recent experiments arrived at different conclusions for the initial conditions [7–9]. Furthermore, nonadiabaticity plays a crucial role. For example, in the attoclock experiment, the ionization time can be mapped to the final angle of the momentum vector in the plane of polarization of the nearly circularly polarized driven laser fields [10,11] if assuming a zero initial momentum $\mathbf{p}(t_i) = 0$ at the exit as in an adiabatic approximation. However, if the initial momentum is nonzero due to nonadiabatic dynamics, the offset angle will be different and so is the retrieved tunneling time. How much nonadiabaticity has to be included in such studies remains unresolved. Conventionally, the Keldysh parameter $\gamma = \omega\sqrt{(2I_p)}/E$ is used for distinguishing the ionization regime with small $\gamma \ll 1$ for tunneling and large $\gamma \gg 1$ for multiphoton ionization; here, ω is the carrier angular frequency, I_p the ionization potential, and E the field strength. At the crossover regime of $\gamma \sim 1$, some experiments indicated [12] that tunneling ionization starts to deviate from the adiabatic limit to nonadiabatic dynamics, which also manifests itself on different tunneling initial conditions. Quantitatively,

the Keldysh parameter is not useful for evaluating the adiabaticity of tunneling. Several theoretical pictures have been put forward based on a semiclassical model [10,11,13], including the electron under-the-barrier motion with complex saddle time [14–16], and using an analytical R matrix method [17,18], to interpret the attoclock experiment, but the results on the adiabaticity of tunneling are still inconclusive. Moreover, recent experiments, by measuring the ionization rate, the spin polarization of an ionized electron, and the bicircular high-harmonic spectroscopy in different atomic species [19–21], suggested that the tunneling probability and velocity are sensitive to the initial quantum states [22–24]. It should be noted that in the original adiabatic Ammosov-Delone-Krainov (ADK) and nonadiabatic Perelomov-Popov-Terentev (PPT) theories [25–28], orbital helicity was not explicitly treated. Considering that most of the experiments were performed on atoms with different contributing orbitals and with laser intensities and wavelengths far away from the pure adiabatic regime (static field), a full account of both the orbital-specific dynamics and the adiabaticity of tunneling is of paramount importance for resolving the discrepancy between different theoretical and/or experimental approaches.

One popular approach is to solve the time-dependent Schrödinger equation (TDSE) for exact solutions [29]. However, it is difficult to extract classical physical insight from such calculations alone. Recently, a virtual detector (VD) technique was proposed to link the time-dependent quantum probability flux to the classical position and momentum [30,31]. For this, one needs to convert the the wave function $\Psi(\mathbf{r}, t)$ to the local momentum through (atomic units are used throughout this paper):

$$\mathbf{p}(\mathbf{r}, t) = \frac{\mathbf{J}(\mathbf{r}, t)}{|\Psi(\mathbf{r}, t)|^2}, \quad (1)$$

where $\mathbf{J}(\mathbf{r}, t) = \frac{i}{2}[\Psi(\mathbf{r}, t)\nabla\Psi(\mathbf{r}, t)^* - \text{c.c.}]$ is the probability flux. By locating the VD at the tunnel exit, the electron's time of arrival at the tunnel exit as well as its exit momentum was determined [32–34]. However, the extracted ionization times are sensitively dependent on how the tunnel exits are chosen, which is not known for nonadiabatic tunneling.

In this work, we introduce a model, which combines the advantages of both TDSE and classical methods, as schematically shown in Fig. 1, to extract the initial conditions of tunneled

*wli@chem.wayne.edu

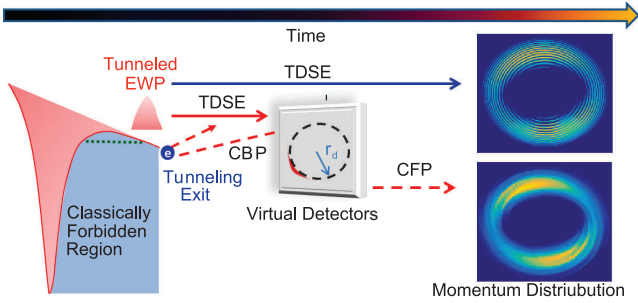


FIG. 1. Schematic representation of the TDSE-CFP and the TDSE-CBP. The TDSE launches an electron wave packet (EWP) in a combined Coulomb potential and laser electric field. The ionized outgoing electron wave packet registers at VDs and then is converted into classical electrons. These electrons are propagated forwards to achieve consistent results with the TDSE, or they are propagated backwards to obtain the tunneling initial conditions.

electrons and to probe the adiabaticity of tunneling ionization. In our method, the outgoing electron wave packet calculated by numerical integration of the TDSE is converted into local momentum $\mathbf{p}(\mathbf{r}_d, t)$ at a circle of radius r_d , and the VDs are evenly arranged on this circle. The local momentum is then propagated forwards to the end of the laser pulse classically for reaching an asymptotic state, or it is propagated backwards to search for tunneling initial conditions. The propagation is preformed under the same Hamiltonian of the TDSE and thus automatically accounts for the Coulomb correction. Moreover, the full quantum treatment before the transformation by VDs enables us to start the calculation from different initial orbitals, without any specific approximations. We term these TDSE based classical forward and backward propagation approaches as TDSE-CFP and TDSE-CBP, respectively. For the forward propagation, the final momentum distribution is achieved by binning electrons with similar momenta, whose probability is summed by the relative weight of each electron's trajectory. For the back propagation, the classical trajectories are terminated with the criterion that the electron has tunneled at time t_0 if the electron's displacement in the instantaneous field direction is a minimum [35]. This criterion is justified because the potential barrier becomes impenetrable for classical particles beyond the tunneling exit when the particles are back propagated from the position of the VD toward the nuclei. Once the tunneling exits are found, the initial momentum as well as the tunneling time can be quantified. The nonadiabatic effect is automatically included in this approach through accurate TDSE calculations and can be characterized by comparing the initial conditions at different wavelengths, as we will show later. Classical back propagation from asymptotic TDSE momentum has been applied previously to resolve the tunneling time [35]. One important advantage of adopting the VD method is the improved computing efficiency, which allows us to calculate the ionizations driven by long wavelength lasers.

II. RESULTS AND DISCUSSION

We first calculate ionized electron momentum distributions of argon atoms using the TDSE-CFP. For argon in the ground-state electron configuration, there are three degenerate

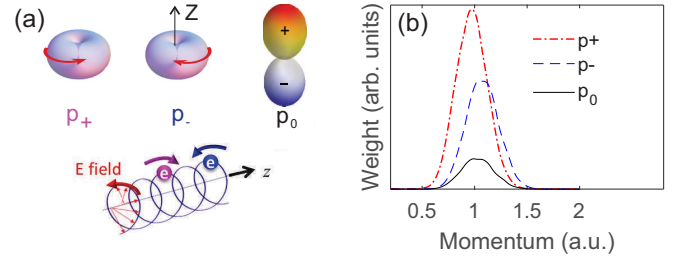


FIG. 2. (a) Illustration of the p orbitals of argon. The three initial orbitals prepared for solving the TDSE are $p_+ = (p_x + ip_y)/\sqrt{2}$, $p_- = (p_x - ip_y)/\sqrt{2}$, and p_0 approximated by an isotropic s orbital with the same eigenenergy, respectively. The electron ring current of the p_+ (p_-) orbital is clockwise (counterclockwise). (b) Radial distributions of momenta calculated by the TDSE-CFP with p_+ , p_0 , and p_- orbitals.

occupied p orbitals, the p_+ ($m = 1$), the p_- ($m = -1$), and the p_0 orbitals ($m = 0$), as shown in Fig. 2(a). The quantum number $m = 1$ ($m = -1$) refers to the projection of the angular momentum in the quantization axis (z axis, light propagation direction), which is 1 (-1), which means the electron ring currents in the polarization plane (xy plane) are counter-rotating (corotating) with respect to the helicity of the driving laser field. We exposed the orbital-specific argon atoms to the left elliptically polarized (LEP) laser field with $\mathbf{E}(t) = \frac{1}{\sqrt{1+\epsilon^2}} E_0 f_e(t) \cos(\omega t + \phi_{\text{CEP}}) \hat{x} + \frac{\epsilon}{\sqrt{1+\epsilon^2}} E_0 f_e(t) \sin(\omega t + \phi_{\text{CEP}}) \hat{y}$, where $\epsilon = 0.89$ is the ellipticity, E_0 is the amplitude and corresponds to a laser peak intensity of 1.2×10^{14} W/cm² ($\gamma \sim 1$), the envelope $f_e(t) = \sin^2(\frac{\pi t}{\tau})$ determines the 30-fs laser pulse duration, ω is the angular frequency refers to a 0.79 μm central wavelength, and ϕ_{CEP} is the carrier envelope phase (CEP) of the laser field. The TDSE $i \frac{\partial \Psi(\mathbf{r}, t)}{\partial t} = [-\frac{\nabla^2}{2} + V_C(\mathbf{r}) + V_E(\mathbf{r}, t)] \Psi(\mathbf{r}, t)$ for the argon atoms is integrated in a two-dimensional grid using the single-active-electron (SAE) approximation. In the equation, the potential terms are given by a time-independent part $V_C(\mathbf{r}) = -\frac{[1 + A \exp(-r^2)]}{\sqrt{r^2 + B}}$ accounting for the Coulomb potential and a time-dependent interaction part $V_E(\mathbf{r}, t) = \mathbf{r} \cdot \mathbf{E}(t)$, which describes the dipole potential in the external laser field. The potential is similar to the empirical three-dimensional potential in [36,37], but due to the lower dimensionality the coefficients of the exponential function are modified for correctly reproducing the eigenenergy of 0.579 a.u. for argon. The basis set of p_x and p_y is obtained via propagation of the TDSE in imaginary time (time step $i\delta t$) and additional orthogonalization procedures at each step. In analogy to the a raising or lowering operator, known as ladder operators, the two degenerate p orbitals of argon can be defined by $p_+ = (p_x + ip_y)/\sqrt{2}$ and $p_- = (p_x - ip_y)/\sqrt{2}$ [38]. Starting from the obtained initial orbitals, we then used the split-step Fourier method to numerically solve the TDSE. The ionized two-dimensional wave function $\Psi(r = \sqrt{x^2 + y^2}, t)$ is saved at the fixed radius r_d , where the virtual detectors are evenly located. The r_d is chosen to be large enough (more than 1.5 times the electron quiver radius in the laser field) to suppress multiple visits of electrons to the VDs, the influence from highly lying states, and any other near-field effects. We also

check that the results do not change if the VDs are located at larger radii, but more computing resources are required. The linear density of VDs defined by $N/2\pi r_d$ is set to 1.6 per arc length for keeping sufficient precision, where N is the number of adopted VDs. We emphasize that the wave packet does not stop at VDs but is propagated beyond VDs continuously until it reaches an absorbing potential to prevent reflection. The absorbing function f_{abs} is in a form of $f_{abs}(\mathbf{r}) = \{\cos[(\mathbf{r} - \mathbf{r}_d)/(\pi/2r_a)]\}^{1/8}$, where $r_a = 20$ represents the range of absorbing function [39]. For each spatial dimension, the grid on which the TDSE is solved should be fine enough to include the detailed evolution of the electron wave packet ($\delta x = \delta y = 0.1$ a.u. in this work). In principle, the grid size should be quite large (thousands of a.u.) because of the outgoing motion of emitted electrons but this has proven to be too resource demanding. However, using the VDs in combination with the absorbing function, it is possible to implement a precise conversion of the wave function to the local momentum at VDs within a range of $2|r_d + r_a|$. This method is more efficient, especially for investigating the problem with long-wavelength driving lasers, which can propagate the electrons to tens of thousands of a.u. away from the ion due to the huge ponderomotive energy. By integrating the momentum distribution over the angle, as shown in Fig. 2(b), the momentum spectra of p_+ , p_0 , and p_- orbitals predicted by TDSE-CFP shows peaks at different momenta. Another interesting feature is that the integrated spectral intensity of the p_+ orbital is several times higher than that of the p_- orbital, which agrees well with previous experimental and theoretical results [19,20,22]. The p_0 orbital has a node in the polarization plane of the electric field, and therefore its contribution to ionization is much lower.

Furthermore, from the calculation, we noted that the angular offsets θ , each of which is defined as the angle between the minor axis (y axis) and the peak angle of photoelectron distributions, are orbital specific, as shown in Fig. 3. By integrating the momentum distribution over the radial direction, we have identified the difference between the offset angles contributed by the laser peak for p_+ and p_- orbitals is ≈ 9.2 deg, as shown in Fig. 3. Similar results were obtained by Smirnova and co-workers in the pioneering work of extending PPT theory to include long-range interaction [22,23]. It is widely accepted that Coulomb attraction is the most important factor that deflects the outgoing electrons, which has been observed as an offset angle between the maximum of the momentum distribution and the minor axes of the polarization ellipse. When the Coulomb potential is turned off, the final direction of both electrons from p_+ and p_- orbitals show almost no deflection. On the other hand, the 12.9° and 22.1° offset angles are observed for the two orbitals if we turn on the Coulomb potential, as shown in Figs. 3(a) and 3(b). One possible and intuitive explanation attributes the disparity to the different tunneling initial velocities. The counter-rotating electron (ionized from the p_+ orbital) escapes from the barrier with a smaller transverse velocity, moves away slower, and is strongly affected by the Coulomb field. The faster corotating electron (ionized from the p_- orbital) weakly interacts with the Coulomb field and is therefore deflected weaker [23,40]. However, previous work predicted a different variation of the two orbitals' offset angle ($\Delta\phi_{off}$). The $\Delta\phi_{off}$

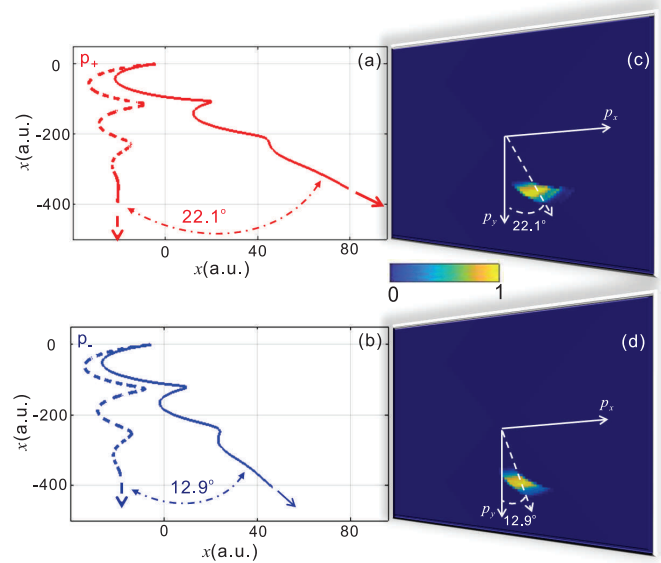


FIG. 3. Classical electron trajectories after tunneling ionization; the electrons are launched by the peak of the elliptically polarized laser. In the left side, (a) and (b) depict one typical trajectory for an electron ionized from p_+ and p_- orbitals, respectively. The solid (dashed) line represents the electron motion with (without) the Coulomb force. The arrows indicate the final direction of the electron momentum after the laser pulse. The right side show the final momentum distribution of electrons ionized within an interval of a 0.1 optical cycle around the laser peak for (c) p_+ and (d) p_- orbitals.

is 2.5° for argon at a laser intensity of 1.2×10^{14} W/cm² in Ref. [23], while it is 12.5° for neon at 1.4×10^{14} W/cm² in Ref. [40]. This disparity prompted us to investigate further into the origin of ionization for a better understanding.

Though the TDSE-CFP calculations provide us reliable results for final momentum distributions, which are consistent with the TDSE solution, the interpretation of them, such as the deviation of the photoelectron distribution maximum and momentum spread, has to rely on the tunneling initial conditions. To reconstruct these initial conditions, the TDSE-CBP was developed.

In the TDSE-CBP, the electron trajectories start from the time when the electrons are registered at VDs (t_{VD}) as shown in Fig. 4(a). The electrons are propagated backwards classically, again with the same Hamiltonian as in the TDSE. But when do we terminate the trajectories and can we find true tunneling exits? Indeed, in classical mechanics, a particle of energy less than the height of a barrier could not penetrate: the region inside the barrier is classically forbidden and this provides a natural termination point (tunneling exit) for the back-propagated classical electrons. For the j th electron, the candidate of the tunneling exit $\mathbf{r}_j(t)$ meets $r_{//,j}(t) = 0$, where $r_{//,j}$ describes the displacement along the instantaneous laser field direction. In Fig. 4(b), we show a typical back-propagated trajectory, in which the electron is ‘‘bounced’’ by the barrier and the tunneling exit is identified. More specifically, the electron first departs from the VD and moves toward the ion core under the reversed laser field. At the very beginning, the

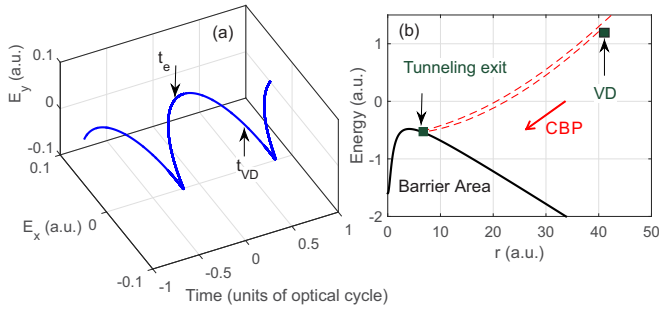


FIG. 4. (a) Evolution of the laser field with time. The zero time corresponds to the laser peak. t_{VD} indicates the instant that an electron is captured by the VDs, and t_e denotes the reconstructed ionization time via the TDSE-CBP. (b) An example shows how a tunneling ionized electron is reflected by the barrier during the CBP, in the energy-distance coordinate system.

electron's energy $E_e(\mathbf{r}, t) = V_C(\mathbf{r}) + V_E(\mathbf{r}, t) + p(\mathbf{r}, t)^2/2$ is much higher than the barrier tail, and therefore it is a free particle, where $p(\mathbf{r}, t)^2/2$ denotes its kinetic energy. When the electron is approaching ion core, $E_e(\mathbf{r}, t)$ gradually drops until it's lower than the barrier top, and it then becomes impossible to move any closer to the ion core. At this instant, the electron is stopped along the laser field and then reflected. The turning point is identified as the tunneling exit. The CBP approach for seeking the tunneling exit requires sufficiently thick tunneling barriers, restricting available laser intensities to $< 2 \times 10^{14}$ W/cm², for the slightly elliptically polarized field used in the current study (argon atom). Higher intensities lead to electron dynamics close to or even over the barrier, which is beyond tunneling ionization. Furthermore, the nonadiabatic dynamics increase the energy of tunneled electrons, which also limits the available laser intensity for performing such calculations.

With TDSE-CBP calculations we can now investigate the origins of orbital specific deviation angles by reconstructing the initial conditions of tunneling ionization. We first reconstructed the initial transverse tunneling momentum, shown in Fig. 5(a), which reads as -0.24 , -0.18 , and -0.12 a.u. for p_+ , p_0 , and p_- orbitals, respectively. Even though the binding electrons in p_+ and p_- orbitals have opposite helicities, once they are ionized, they will have the same corotating

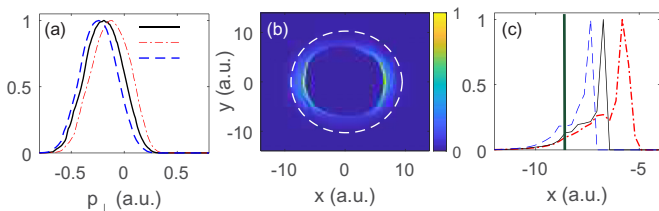


FIG. 5. (a) The reconstructed normalized initial transverse momentum distribution for p_+ , p_0 , and p_- orbitals. (b) The initial ionization position calculated with the TDSE-CBP method (density plot), and Landau's effective potential theory (dashed white), launched from the p_0 orbital. (c) The comparison of the ionization position for p_+ , p_0 , and p_- orbitals and the Landau model (solid green), along the vector direction of the laser peak.

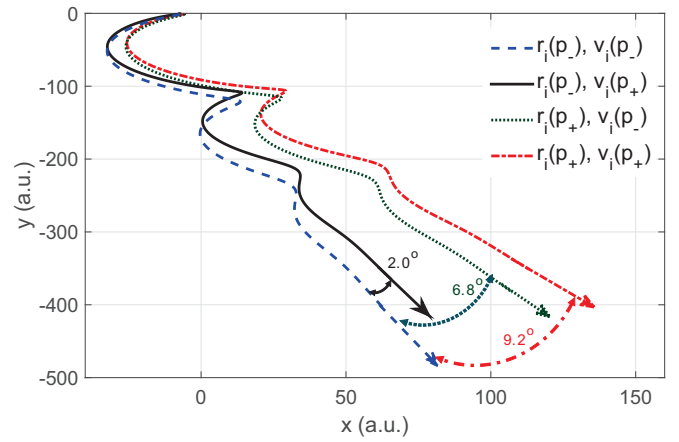


FIG. 6. The comparison of electrons' classical trajectories and angles of deviation for different tunneling initial positions $r_i(x_i, y_i)$ and velocities $v_i(v_{xi}, v_{yi})$. The noted p_+ or p_- in brackets denotes that the r_i or v_i is adopted from the corresponding orbital.

initial momentum with the laser field. The same sign of the initial momentum shows momentum (energy) has to be gained during the tunneling process, i.e., a nonadiabatic effect. In the semiclassical model such as in [15], the nonadiabatic tunneling dynamics is accompanied by a shift of the tunneling exit towards the ionic core, as a consequence of the absorption of energy from the laser field. In Fig. 5(b), we confirm this is indeed the case by reconstructing the tunneling exits by the TDSE-CBP method for the p_0 orbital as an example. The tunneling exit is located closer to the ionic core, compared to the predictions by Landau's effective potential theory in the adiabatic regime [41]. More interestingly, we found different tunneling exit locations for p_+ , p_0 , and p_- along the laser peak vector (negative x axis) in Fig. 5(c), even though the ionization potentials and laser parameters are exactly the same for all three orbitals. This result turns out to be the major reason for the orbital-dependent offset angles: the closer to nucleus the electron is born, the stronger Coulomb interaction there is, thus a stronger deflection for the p_+ orbital; see Fig. 6.

In Fig. 6, we exchange the tunneling initial velocity and position for the p_- orbital to those of the p_+ orbital artificially, and then analyze the electron's behaviors. The tunneling initial position and velocity for the most probable electrons for the two orbitals can be read out from Fig. 5. When only the initial velocity of the p_- orbital is replaced by that of the p_+ orbital, while the initial ionization position is maintained, a deviation angle of 2.0° is observed. If we only replace the p_- orbital's initial position by the p_+ orbital's, the deviation angle is 6.8° . This can be easily understood that the Coulomb force strongly affects the electron launched at the inner position. Finally when we change both the initial position and velocity, a deviation angle of 9.2° is obtained. The comparison of electrons' classical trajectories and angles of deviation stated above are shown in Fig. 6. Therefore, not only the orbital-specific tunneling initial transverse velocity, but also the shift of tunneling coordinates arising from nonadiabatic dynamics, plays an important role in deflecting electrons from p_+ and p_- orbitals to different angles.

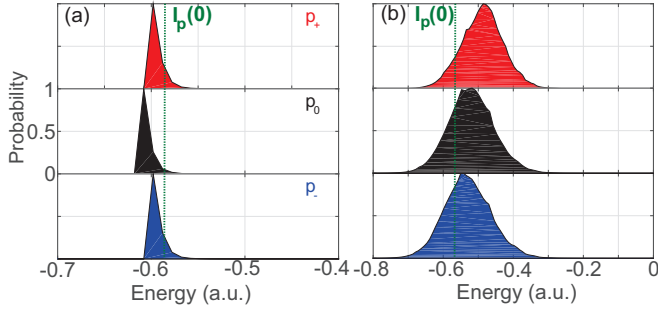


FIG. 7. The reconstructed energy distribution of electrons at the tunneling exit for p_- , p_0 , and p_+ orbitals in (a) the quasistatic laser field and (b) the slightly elliptically polarized laser field.

We note because the instant of ionization correlates with the angle of photoemission through $\theta_\tau = \omega\tau$ (τ is the ionization delay time with respect to the laser peak) in the angular streaking experiment, we need to compare the ionization times for the three orbitals. We observed a close-to-zero tunneling delay for all three orbitals, similar to what was previously concluded [14,35]. Therefore, the orbital-specific offset angles can not be attributed to the differences in the tunneling time.

Furthermore, the closest tunneling exit location for the p_+ orbital means the electron acquires the most energy from the laser field among the three orbitals. This is further confirmed by the reconstructed energies at the tunneling exit for these three orbitals in Fig. 7. When an atom is exposed to a laser field, it is polarized, and its ionization potential will be affected via the well-known Stark shift. In a static electric field F , the Stark shift can be calculated by [42,43] $I_p(F) = I_p(0) + \frac{1}{2}\alpha_N F^2$, where $I_p(0) = 0.579$ a.u. is the field-free ionization energy of argon, and $\alpha_N = 11.1$ [44] is the static atomic polarizability. The ionic polarizability α_I is absent because the potential in a TDSE calculation does not include the core polarization effect, leading to a slightly overestimated Stark shift. The linear Stark shift term is not taken into account here, because the considered argon atom has no permanent dipole moment. For comparison, we first study the static case by adopting a 10-fs \sin^2 envelope laser field without a carrier wave. The peak intensity of the laser field is still 1.2×10^{14} W/cm². The electron's energies at the tunneling exit are reconstructed for p_- , p_0 , and p_+ orbitals by performing the TDSE-CBP with this quasistatic laser field, as shown in Fig. 7(a). We note that the most probable energy of an electron tunneled from the p_0 orbital is -0.603 a.u., which is consistent with the results predicted by considering the static Stark shift. On the other hand, the electron tunneled from p_- and p_+ orbitals tends to gain more energy but is still lower than $I_p(0)$. This can be explained by the initial transverse momentum of the p_- or p_+ electron shown in Fig. 5(a). The degeneracy of the p_+ and p_- ionization energy level is guaranteed by the perturbation theory. We next turn to the case of using a slightly elliptically polarized driving laser with the same intensity as the quasistatic case. In Fig. 7(b), one can see that the most probable ionization energies are raised higher than $I_p(0)$ for all of the three orbitals. During tunneling ionization, the electron gains energy from the varying barrier, and it is converted to the potential energy and kinetic energy of the electron. The additional

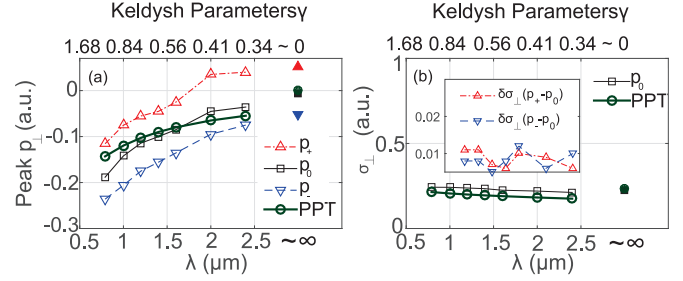


FIG. 8. (a) The most probable transverse momentum at the tunneling exit p_\perp vs the Keldysh parameter. (b) The reconstructed width of the initial transverse momentum σ_\perp as a function of the Keldysh parameter. The transverse momentum distribution is assumed to have the form $\exp(-p_\perp^2/\sigma_\perp^2)$. The inset shows a zooming in differences between the momentum width of p_+ and the momentum width of p_0 and p_- and p_0 . The laser intensity is maintained at 1.2×10^{14} W/cm², and the corresponding γ for the wavelengths varies from 1.06 to 0.36. The solid marks represent the quasistatic limitation by using a 10-fs \sin^2 envelope laser field without a carrier wave.

kinetic energy is related to the nonzero momentum observed at the tunneling exit as indicated in Fig. 5(a). An intuitive physical picture for the raising of energy is the shift of the tunneling exit toward the ion core, because the ionization takes place closer to the barrier top. Moreover, the change of the ionization energy also implies how the ionization probability is modified. From the point of view of the strong field approximation (SFA) and the imaginary time under-barrier motion, the transition rate from the ground state to a continuum state can be represented as $\Gamma = \exp[-2\text{Im}(S_S + S_C)]$, where $S_S = \int_{t_s}^{t_0} dt \{[\mathbf{p} + \mathbf{A}(t)]^2 + I_p\}$ is the classical action under the barrier and $S_C = \int_{t_s}^{t_0} dt V[\mathbf{r}(t)]$ is its Coulomb correction [15,27,45]; \mathbf{p} and $\mathbf{A}(t)$ are the canonical momentum and vector potential, respectively. As pointed out in [15], this integration for S is related to the area between the potential barrier and the ionization energy level. Because the ionization from the p_+ orbital exhibits a bigger upshift of energy compared to the p_- orbital case, the mentioned area is therefore smaller, which results in a higher ionization probability, providing an alternative explanation to the experimentally observed helicity dependent ionization rates in the nonadiabatic tunneling regime [19]. An exception for the above explanation is the case of the p_0 orbital, because the SFA theory can not account for the orbital structure. The nodal in the laser polarization plane for the p_0 orbital gives rise to the lowest ionization probability.

Now we move to characterize the adiabaticity of tunneling under different laser conditions (the Keldysh parameters γ). We use the central wavelengths of the driving laser as a knob to vary γ , and then the nonadiabaticities are examined by reconstructing the peak and width of the initial transverse momentum. For comparison, a calculation with a quasistatic laser field was also carried out to provide a baseline of adiabatic tunneling ($\gamma = 0$). In principle, one can vary γ by changing the laser intensity. However, higher intensities could lead to over-the-barrier ionization, in which the concept of tunneling can not apply anymore. In Fig. 8(a), we compare the peak position

of the initial transverse momentum for p_+ and p_- orbitals at different γ values. With a decreasing γ , the most probable transverse momenta for three orbitals approach steadily toward their own quasistatic limits (solid marks), exhibiting a reducing nonadiabaticity. The p_0 orbital shows a very similar behavior compared with the prediction of the nonadiabatic PPT method [27,28]. It is surprising that nonadiabaticity can persist well beyond $\gamma < 0.5$ and a laser wavelength $> 1.6 \mu\text{m}$. It is interesting to note that even at the adiabatic limit, there is a nonvanishing initial transverse momentum for orbitals with a nonzero magnetic quantum number and the direction of the initial transverse momentum matches the helicities of the orbitals. It is also worth noting that the differences between p_+ , p_0 , and p_- orbitals at each γ are almost constant as γ decreases, implying a similar nonadiabatic effect on the peak value of the transverse momentum for all three orbitals. On the other hand, it seems nonadiabatic dynamics has little effect on the width of the initial transverse momentum distribution σ_{\perp} and shows the same trend as the PPT model, as shown in Fig. 8(b).

III. CONCLUSION

We have identified the orbital effect on photoelectron momentum distribution in nonadiabatic tunneling ionization with the help of TDSE-CFP and TDSE-CBP methods. We further identified the initial transverse momentum as a sensitive probe of the adiabaticity of tunneling ionization. The improved understanding of the nonadiabatic tunneling should help clarify existing controversies in tunneling initial conditions and is important for quantitative interpretation of attoclock experiments. TDSE-CFP and TDSE-CBP methods can be extended to more complex orbitals, and it will be interesting to apply this approach to study tunneling dynamics in molecules [46] and multielectron dynamics.

ACKNOWLEDGMENTS

This research is supported by the Chemical Sciences, Geosciences, and Biosciences Division, Office of Basic Energy Sciences, Office of Science, U.S. Department of Energy under Grant No. DE-SC0012628.

-
- [1] F. Krausz and M. Ivanov, *Rev. Mod. Phys.* **81**, 163 (2009).
- [2] R. Boge, C. Cirelli, A. S. Landsman, S. Heuser, A. Ludwig, J. Maurer, M. Weger, L. Gallmann, and U. Keller, *Phys. Rev. Lett.* **111**, 103003 (2013).
- [3] N. I. Shvetsov-Shilovski, D. Dimitrovski, and L. B. Madsen, *Phys. Rev. A* **85**, 023428 (2012).
- [4] A. N. Pfeiffer, C. Cirelli, M. Smolarski, D. Dimitrovski, M. Abu-samaha, L. B. Madsen, and U. Keller, *Nat. Phys.* **8**, 76 (2012).
- [5] M. Meckel, D. Comtois, D. Zeidler, A. Staudte, D. Pavičić, H. C. Bandulet, H. Pépin, J. C. Kieffer, R. Dörner, D. M. Villeneuve, and P. B. Corkum, *Science* **320**, 1478 (2008).
- [6] J. Maurer, D. Dimitrovski, L. Christensen, L. B. Madsen, and H. Stapelfeldt, *Phys. Rev. Lett.* **109**, 123001 (2012).
- [7] L. Arissian, C. Smeenk, F. Turner, C. Trallero, A. V. Sokolov, D. M. Villeneuve, A. Staudte, and P. B. Corkum, *Phys. Rev. Lett.* **105**, 133002 (2010).
- [8] D. Shafir, H. Soifer, B. D. Bruner, M. Dagan, Y. Mairesse, S. Patchkovskii, M. Yu. Ivanov, O. Smirnova, and N. Dudovich, *Nature (London)* **485**, 343 (2012).
- [9] A. N. Pfeiffer, C. Cirelli, A. S. Landsman, M. Smolarski, D. Dimitrovski, L. B. Madsen, and U. Keller, *Phys. Rev. Lett.* **109**, 083002 (2012).
- [10] P. Eckle, A. N. Pfeiffer, C. Cirelli, A. Staudte, R. Dörner, H. G. Muller, M. Büttiker, and U. Keller, *Science* **322**, 1525 (2008).
- [11] P. Eckle, M. Smolarski, P. Schlup, J. Biegert, A. Staudte, M. Schöffler, H. G. Muller, R. Dörner, and U. Keller, *Nat. Phys.* **4**, 565 (2008).
- [12] M. Uiberacker, Th. Uphues, M. Schultze, A. J. Verhoef, V. Yakovlev, M. F. Kling, J. Rauschenberger, N. M. Kabachnik, H. Schröder, M. Lezius, K. L. Kompa, H.-G. Muller, M. J. J. Vrakking, S. Hendel, U. Kleineberg, U. Heinzmann, M. Drescher, and F. Krausz, *Nature (London)* **446**, 627 (2007).
- [13] A. S. Landsman, C. Hofmann, A. N. Pfeiffer, C. Cirelli, and U. Keller, *Phys. Rev. Lett.* **111**, 263001 (2013).
- [14] L. Torlina, F. Morales, J. Kaushal, I. Ivanov, A. Kheifets, A. Zielinski, A. Scrinzi, H. G. Muller, S. Sukiasyan, M. Ivanov, and O. Smirnova, *Nat. Phys.* **11**, 503 (2015).
- [15] M. Klaiber, K. Z. Hatsagortsyan, and C. H. Keitel, *Phys. Rev. Lett.* **114**, 083001 (2015).
- [16] M. Li, J. W. Geng, M. Han, M.-M. Liu, L.-Y. Peng, Q. Gong, and Y. Liu, *Phys. Rev. A* **93**, 013402 (2016).
- [17] L. Torlina and O. Smirnova, *Phys. Rev. A* **86**, 043408 (2012).
- [18] J. Kaushal and O. Smirnova, *Phys. Rev. A* **88**, 013421 (2013).
- [19] T. Herath, L. Yan, S. K. Lee, and W. Li, *Phys. Rev. Lett.* **109**, 043004 (2012).
- [20] D. Baykusheva, M. S. Ahsan, N. Lin, and H. J. Wörner, *Phys. Rev. Lett.* **116**, 123001 (2016).
- [21] A. Hartung, F. Morales, M. Kunitski, K. Henrichs, A. Laucke, M. Richter, T. Jahnke, A. Kalinin, M. Schöffler, L. P. H. Schmidt, M. Ivanov, O. Smirnova, and R. Dörner, *Nat. Photon.* **10**, 526 (2016).
- [22] I. Barth and O. Smirnova, *Phys. Rev. A* **84**, 063415 (2011).
- [23] J. Kaushal, F. Morales, and O. Smirnova, *Phys. Rev. A* **92**, 063405 (2015).
- [24] K. Liu and I. Barth, *Phys. Rev. A* **94**, 043402 (2016).
- [25] M. V. Ammosov, N. B. Delone, and V. P. Krainov, *Sov. Phys. JETP* **64**, 1191 (1986).
- [26] A. M. Perelomov, V. S. Popov, and M. V. Terent'ev, *Sov. Phys. JETP* **50**, 1393 (1966).
- [27] A. M. Perelomov and V. S. Popov, *Sov. Phys. JETP* **25**, 336 (1967).
- [28] G. L. Yudin and M. Y. Ivanov, *Phys. Rev. A* **64**, 013409 (2001).
- [29] I. A. Ivanov and A. S. Kheifets, *Phys. Rev. A* **89**, 021402(R) (2014).
- [30] B. Feuerstein and U. Thumm, *J. Phys. B* **36**, 707 (2003).
- [31] X. Wang, J. Tian, and J. H. Eberly, *Phys. Rev. Lett.* **110**, 243001 (2013).
- [32] N. Teeny, E. Yakaboylu, H. Bauke, and C. H. Keitel, *Phys. Rev. Lett.* **116**, 063003 (2016).

- [33] N. Teeny, C. H. Keitel, and H. Bauke, *Phys. Rev. A* **94**, 022104 (2016).
- [34] I. Barth and M. Lein, *J. Phys. B: At., Mol. Opt. Phys.* **47**, 204016 (2014).
- [35] H. Ni, U. Saalmann, and J-M. Rost, *Phys. Rev. Lett.* **117**, 023002 (2016).
- [36] X. Tong and C. D. Lin, *J. Phys. B* **38**, 2593 (2005).
- [37] Q. Zhang, P. Lan, and P. Lu, *Phys. Rev. A* **90**, 043410 (2014).
- [38] S. Bauch and M. Bonitz, *Phys. Rev. A* **78**, 043403 (2008).
- [39] H. Yu and A. D. Bandrauk, *Phys. Rev. A* **56**, 685 (1997).
- [40] Y. Li, P. Lan, H. Xie, M. He, X. Zhu, Q. Zhang, and P. Lu, *Opt. Express* **23**, 28801 (2015).
- [41] L. D. Landau and E. M. Lifshitz, *Quantum Mechanics* (Pergamon, Oxford, 1977).
- [42] D. Dimitrovski, M. Abu-samha, L. B. Madsen, F. Filsinger, G. Meijer, J. Küpper, L. Holmegaard, L. Kalthøj, J. H. Nielsen, and H. Stapelfeldt, *Phys. Rev. A* **83**, 023405 (2011).
- [43] D. Dimitrovski, C. P. J. Martiny, and L. B. Madsen, *Phys. Rev. A* **82**, 053404 (2010).
- [44] V. Shevelko and A. Vinogradov, *Phys. Scripta* **19**, 275 (1979).
- [45] W. Becker, F. Grasbon, D. Kopold, D. B. Milošević, G. G. Paulus, and H. Walther, *Adv. At. Mol. Opt. Phys.* **48**, 35 (2002).
- [46] C. Xie, J. Ma, X. Zhu, D. R. Yarkony, D. Xie, and H. Guo, *J. Am. Chem. Soc.* **138**, 7828 (2016).